Journal of
Materials Chemistry A

PAPER

Cite this: DOI: 10.1039/c6ta06430b

Pd_2Sn [010] nanorods as a highly active and stable ethanol oxidation catalyst

Zhishan Luo,†[a] Jianmin Lu,†[b] Cristina Flox,*[a] Raquel Nafria,[a] Aziz Genç,[c] Jordi Arbiol,[cd] Jordi Llorca,[e] Maria Ibáñez,[a] Joan Ramon Morante[af] and Andreu Cabot*[ad]

Received 28th July 2016
Accepted 5th October 2016

DOI: 10.1039/c6ta06430b

www.rsc.org/MaterialsA

The development of highly active, low cost and stable electrocatalysts for direct alcohol fuel cells remains a critical challenge. While Pd_2Sn has been reported as an excellent catalyst for the ethanol oxidation reaction (EOR), here we present DFT analysis results showing the (100) and (001) facets of orthorhombic Pd_2Sn to be more favourable for the EOR than (010). Accordingly, using tri-*n*-octylphosphine, oleylamine (OLA) and methylamine hydrochloride as size and shape directing agents, we produced colloidal Pd_2Sn nanorods (NRs) grown in the [010] direction. Such Pd_2Sn NRs, supported on graphitic carbon, showed excellent performance and stability as an anode electrocatalyst for the EOR in alkaline media, exhibiting 3 times and 10 times higher EOR current densities than that of Pd_2Sn and Pd nanospheres, respectively. We associate this improved performance with the favourable faceting of the NRs.

Introduction

Ethanol is a particularly appealing fuel. Ethanol (24 MJ L^{-1}) has higher energy density than hydrogen (liquid, 8.5 MJ L^{-1}), methanol (15.6 MJ L^{-1}) or formic acid (6.4 MJ L^{-1}). It has a low toxicity, is safe to store due to its relatively high boiling point and can be bio-sourced by fermentation of sugar- or cellulose-containing compounds.[1–6] Therefore, direct ethanol fuel cells (DEFCs), with low operating temperature , high potential energy density, and safe storage and operation, are considered as one of the main candidate technologies to supply electric power in electric vehicles and portable electronics.[7] However, several limitations still hinder the large scale implementation of DEFCs, most of them being related to the ethanol oxidation electrocatalyst. Current electrocatalysts for the ethanol oxidation reaction (EOR) show relatively slow kinetics and low stability associated with the poisoning of the surface active sites. The use of alkaline media represents an advantage in these two directions. Compared with acid electrolytes, alkaline solutions provide faster reaction kinetics for both alcohol oxidation and oxygen reduction, enabling the use of less expensive catalysts or higher efficiencies in the use of precious metals, easier electrolyte management and a wider fuel product selection.[6,8–11] Pt has been widely used as the most active electrocatalyst for DEFCs.[12–17] However, its scarcity and relatively high price limit the cost-effectiveness of this technology. Recently, increasing attention has been paid to less expensive Pd and Pd-based compounds which show comparable or even better electrocatalytic activities than Pt-based catalysts for alcohol oxidation.[18–20] Specifically, alloying Pd with elements such as Sn,[21–24] Co,[25] Cu[26,27] or Bi[28] is effective in increasing electrocatalytic activity and CO tolerance, particularly for the EOR.

Currently, electrocatalysts are mainly produced by the impregnation, electrodeposition or evaporation of one or several active phases on a large surface support. These methodologies provide very limited control over the size, shape and distribution of the different phases, which generally makes the development of new catalysts a slow trial and error process, especially in structure sensitive reactions such as the EOR. Alternatively, colloidal synthesis routes and bottom-up assembly procedures allow an unmatched precise tuning over material properties at the nanometer scale. Moreover, such control of material parameters at their lowest organization level does not require high capital cost equipment or extremely complex procedures, but can be reached using high-throughputs and high yield chemical routes at ambient pressure and low temperature. The huge potential of such solution-based strategies to tune material properties resides in the ability

---

[a] *Catalonia Institute for Energy Research-IREC, 08930 Sant Adrià del Besos, Barcelona, Spain. E-mail: cflox@irec.cat; acabot@irec.cat*

[b] *State Key Laboratory of Catalysis, Dalian National Laboratory for Clean Energy, Dalian Institute of Chemical Physics, Chinese Academy of Sciences, Dalian 116023, China*

[c] *Catalan Institute of Nanoscience and Nanotechnology (ICN2), CSIC, The Barcelona Institute of Science and Technology (BIST), Campus UAB, Bellaterra, 08193 Barcelona, Spain*

[d] *ICREA, Pg. Lluís Companys 23, 08010 Barcelona, Spain*

[e] *Institut de Tècniques Energètiques, Universitat Politècnica de Catalunya, 08028 Barcelona, Spain*

[f] *Departament d'Electronica, Universitat de Barcelona, 08028 Barcelona, Spain*

† These authors contributed equally.

to chemically manipulate material formation, from the very initial combination of atoms into clusters to the growth of nanometer scale entities. Chemical manipulation is accomplished through the use of surfactants, which regulate the incorporation of atom/ions at each surface site by locally determining the surface energy and charge. This strategy allows huge amounts of colloidal nanoparticles (NPs) to simultaneously nucleate and grow, all evolving at the same rate under the same conditions. Thus, massive amounts of particles with precisely tuned properties can be produced in a simple, fast and cost-effective manner. Colloidal synthesis routes are also extremely versatile, allowing the production of elemental, multinary and heterostructured NPs with metallic, semiconductor, magnetic, plasmonic, *etc.* character and with unmatched composition, size, shape and phase control.[29–37]

In the present work, using DFT calculations, we show the (100) and (001) facets of orthorhombic Pd_2Sn to be more favorable for the EOR than (010). We subsequently produced colloidal Pd_2Sn NRs grown in the [010] direction and assessed their electrocatalytic performance as an anode EOR electrocatalyst for DEFCs in an alkaline medium, comparing it with that of Pd_2Sn and Pd spherical NPs.

Experimental

Chemicals

Palladium(II) acetylacetonate ($Pd(acac)_2$, 99%), tin(II) acetate ($Sn(OAc)_2$), oleylamine (OLA, >70%), oleic acid (OA, 90%), methylamine hydrochloride (MAHC), and hydrazine hydrate (N_2H_4, 50–60% in water) were purchased from Sigma Aldrich. Tri-*n*-octylphosphine (TOP, 97%) was purchased from Strem. Hexane, chloroform and ethanol were of analytical grade and obtained from various sources. MilliQ water was obtained by using a PURELAB flex from ELGA. All chemicals were used as received without further purification, except OLA, which was purified by distillation. All syntheses were carried out using standard airless techniques: a vacuum/dry argon Schlenk line was used for the syntheses and an argon glove-box was used for storing and handling sensitive chemicals.

Pd_2Sn NRs

Pd_2Sn NRs were prepared following the protocol we previously reported with slight modifications.[24] Briefly, 20 mL of OLA, a certain amount of MAHC, 0.3 mmol of $Pd(acac)_2$ and 0.15 mmol $Sn(OAc)_2$ were placed in a 100 mL four-neck flask and purged under argon flow for 30 minutes at 60 °C. Then 1 mL of TOP was injected into the solution and the solution was heated to 200 °C in 10 min and kept for 30 min. Then, the temperature was further increased to 300 °C in 40 min and maintained for additional 30 min. Finally, the solution was cooled to room temperature. Pd_2Sn NPs were collected by centrifuging and washing with ethanol and chloroform. When different amounts of MAHC were used, different sizes and aspect ratios of NRs were obtained.

Pd_2Sn and Pd spherical NPs were also produced following previously reported procedures with slight modifications.[24] Briefly, Pd_2Sn spherical NPs were obtained by mixing 20 mL of OLA, 0.3 mmol of $Pd(acac)_2$, 0.15 mmol of $Sn(OAc)_2$ and 1 mL of TOP under argon flow but without MAHC. The rest of the procedure was the same as that used to produce Pd_2Sn NRs. Pd spherical NPs were prepared by mixing OLA, $Pd(acac)_2$ and TOP under argon flow but without $Sn(OAc)_2$ and MAHC precursors and then setting the growth temperature to 200 °C and the growth time to 30 min.

Organic ligand removal

Pd_2Sn NPs dispersed in hexane (~50 mg in 5 mL) were mixed with an equal volume fraction of a 1 M hydrazine hydrate aqueous solution to form a two phase system. The mixture was stirred until the black NPs turned into the aqueous phase. NPs were collected by centrifugation and washed with hexane and ethanol.

Characterization

The size and shape of initial NPs were examined by transmission electron microscopy (TEM) using a ZEISS LIBRA 120, operating at 120 kV. The structural and compositional properties of the nanocomposites were also examined by TEM. High resolution TEM (HRTEM) studies were conducted using a field emission gun FEI™ Tecnai F20 microscope at 200 kV with a point-to-point resolution of 0.19 nm. Scanning electron microscopy (SEM) analysis was done on a ZEISS Auriga SEM with an energy dispersive X-ray spectroscopy (EDS) detector at 20 kV to study the composition of nanoparticles. For SEM characterization, NPs were dissolved in chloroform and were drop cast on silicon substrates. Powder X-ray diffraction (XRD) patterns were collected directly from the as-synthesized NPs dropped on the Si(501) substrate on a Bruker AXS D8 Advance X-ray diffractometer with Ni-filtered (2 μm thickness) Cu K radiation ($\lambda = 1.5406$ Å) operating at 40 kV and 40 mA. A LynxEye linear position-sensitive detector was used in reflection geometry. X-ray photoelectron spectroscopy (XPS) was performed on a SPECS system equipped with an Al anode XR50 source operating at 150 mW and a Phoibos 150 MCD-9 detector. The pressure in the analysis chamber was always below 10^{-7} Pa. The area analyzed was about 2 mm × 2 mm. The pass energy of the hemispherical analyzer was set at 25 eV and the energy step was set at 0.1 eV. Data processing was performed with the CasaXPS program (Casa Software Ltd., UK). Binding energy (BE) values were centered using the C 1s peak at 284.8 eV. The atomic fractions (%) were calculated using peak areas normalized on the basis of acquisition parameters after background subtraction, experimental sensitivity factors and transmission factors provided by the manufacturer. Fourier transform infrared spectroscopy (FTIR) was performed on an Alpha Bruker FTIR spectrometer with a platinum attenuated total reflectance (ATR) single reflection module. FTIR data were typically averaged over 64 scans.

Electrochemical measurements

All electrochemical measurements were performed at room temperature in a standard three-electrode cell using a rotating

Table 1 Parameters of 3 Pd_2Sn surface slabs for the DFT calculations. The (010), (001) and (100) slabs are orthorhombic

Surface	Periodicity	*a* (Å)	*b* (Å)	*c* (Å)	Pd atoms	Sn atoms	*k*-Point mesh
(010)	1 × 1 × 2	8.203	5.616	21.500	16	8	5 × 7 × 1
(001)	1 × 1 × 2	11.230	8.667	22.305	32	16	3 × 4 × 1
(100)	2 × 1 × 1.5	8.667	8.203	22.733	24	12	4 × 5 × 1

disc electrode from Pine Instruments connected to a Bio-Logic VMP-3 multipotentiostat controlled by EC-lab software. A Pt foil and Hg/HgO (1 M KOH) were used as counter and reference electrodes, respectively. The working electrode was prepared using a glassy carbon (GC) disc measuring 5 mm in diameter, which was previously polished with diamond (1 μm) and alumina (0.05 μm), sonicated for 10 min and washed with deionized water. Catalytic electrodes were produced by drop-casting 10 μL of a 2 mg mL^{-1} suspension of NPs in deionized water on the GC. To immobilize the Pd or Pd_2Sn NPs on the GC, 10 μL of 0.5 wt% Nafion was dropped on the surface of the electrode. The background was obtained by cyclic voltammetry (CV) in an argon-purged aqueous solution of 0.5 M KOH without ethanol solution from −1 to 0.3 V *vs.* Hg/HgO at 50 mV s^{-1} and 1000 rpm. The electrochemically active surface areas (ECSAs) were evaluated from integration of the charges during PdO reduction in the cathode scan, assuming a value of 405 μC cm^{-2} for the reduction of the PdO monolayer. The electrochemical activity of the Pd- and PdSn-based catalysts was conducted in 0.5 M KOH with 0.5 M ethanol solution under the same conditions. The chronoamperometric (CA) analysis was conducted at −0.1 V for 2 h in 0.5 M ethanol/0.5 M KOH electrolyte in order to elucidate the stability of the NPs. The quasi-steady state polarization curves recorded at a sweep rate of 1 mV s^{-1} by using the Linear Sweep Voltammetry (LSV) technique in 0.5 M ethanol/0.5 M KOH solutions were used to derive the Tafel plots. Current densities were calculated taking into account the geometrical area of the electrode (0.196 cm^{-2}). Electrochemical impedance spectroscopy (EIS) measurements were carried out from 100 kHz to 10 mHz with a 5 mV Ac amplitude at −0.4 and −0.1 V.

DFT calculations

All DFT calculations were performed using the Vienna *Ab initio* Simulation Package (VASP),[38,39] a periodic plane-wave-based density functional theory (DFT) package. The electron–ion interactions were described by the projector-augmented wave method (PAW).[40] The exchange correlation energy has been calculated within the generalized gradient approximation by the Perdew–Burke–Ernzerhof formulation (GGA-PBE).[41,42] The kinetic energy cutoff of plane-wave basis sets was fixed to 400 eV for all calculations. Dispersion (van der Waals forces) corrections were included by the DFT-D3 methodology.[43] The lattice constants of bulk orthorhombic Pd_2Sn were calculated to be $a = 5.616$ Å, $b = 4.333$ Å, and $c = 8.203$ Å, which are in reasonable agreement with experimental values ($a = 5.635$ Å, $b = 4.283$ Å, and $c = 8.091$ Å).[24] These lattice constants are used to construct 3 periodic Pd_2Sn slabs ((010), (001) and (100) surfaces), the parameters of which are listed in Table 1. For each slab, 15 Å of the vacuum layer was added to mitigate the interactions between the slab and its periodic replica. For the 3 slabs, the bottom half atomic layers were fixed to their optimized bulk configuration during all computations, and the top half atomic layers and surface intermediates are fully relaxed. All atomic coordinates of the adsorbates and the atoms in the relaxed layers were optimized to a force of <0.03 eV $Å^{-1}$ on each atom. All self-consistent field calculations were converged to 1×10^{-5} eV. Brillouin zone integration was performed with a Methfessel–Paxton smearing order of 2 with a broadening of 0.2 eV. The adsorption energy of ethanol, E_{ads}, was calculated by the following equation:

$$E_{ads} = E_{slab+ethanol} - E_{slab} - E_{ethanol(g)}$$

where $E_{slab+ethanol}$ is the total energy of the slab with an ethanol bound to it, E_{slab} is the total energy of the clean Pd_2Sn slab, and $E_{ethanol(g)}$ is the total energy of ethanol in the gas phase.

Results and discussion

While the mechanism of electrochemical oxidation of ethanol is still controversial, it is generally accepted that the first step involves the dissociative adsorption of ethanol on the catalyst surface aided by hydroxide groups.[6,44–47] We carried out a DFT investigation of the interaction between the ethanol molecule and different Pd_2Sn surfaces to understand the role of Pd and Sn and different facets in this reaction. Fig. 1 shows the ethanol adsorption configurations on Pd_2Sn (001), (010) and (100) surfaces. The adsorption energies of ethanol (E_{ads}) on Pd obtained for each surface were −0.52, −0.45 and −0.51 eV for Pd_2Sn (001), Pd_2Sn

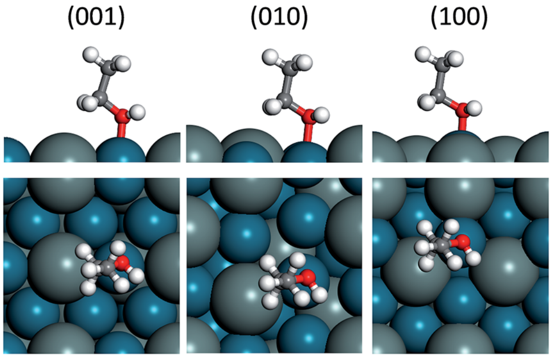

Fig. 1 Side (upper panel) and top views (lower panel) of the preferred adsorption structure of ethanol on Pd atoms over the Pd_2Sn (001), Pd_2Sn (010) and Pd_2Sn (100) surfaces. Blue and dark silver spheres represent Pd and Sn atoms, respectively.

(010) and Pd_2Sn (100), respectively. The corresponding E_{ads} of Sn were −0.35, −0.42 and −0.45 eV, respectively. The higher absolute values of E_{ads} on Pd indicate that ethanol molecules prefer to adsorb on Pd atoms instead of Sn, in which cases, the O atom of ethanol binds on top of Pd atoms. However, the presence of Sn clearly changes E_{ads} of Pd by means of an electronic and also a geometrical effect. Our DFT results also show that among the studied surfaces and taking into account just the first ethanol adsorption step, the (001) and (100) are more favorable for the EOR than the (010). We also investigated the OH^- adsorption on the different elements and facets. DFT calculations showed that OH^- preferentially adsorbs on Sn atoms at (001) and (100) facets, with E_{ads} values −2.91 and −2.92, respectively. E_{ads} on Sn at a (010) facet was just −2.83 and E_{ads} on Pd sites ranged from −2.61 for (010) to −2.27 and −2.25 for (001) and (100) facets, respectively.

Fig. 2a and c show representative TEM micrographs and size distribution histograms of 4 nm spherical Pd NPs, 5 nm spherical Pd_2Sn NPs and different aspect ratio Pd_2Sn NRs produced following the above detailed procedure.[24] Pd_2Sn NRs were synthesized from the reaction of $Pd(acac)_2$ and $Sn(OAc)_2$ in the presence of OLA, TOP and MAHC.[24] Increasingly larger sizes and aspect ratios were obtained by increasing the amount of MAHC added: 9 nm × 26 nm (0.85 mmol MAHC); 10 nm × 70 nm (0.95 mmol MAHC); 12 nm × 150 nm (1.8 mmol MAHC); 20 nm × 460 nm (2.75 mmol MAHC).

HRTEM analysis showed Pd_2Sn NRs to be crystalline with an orthorhombic structure (space group *Pnma*) with $a = 0.56$ Å, $b = 0.431$ Å and $c = 0.812$ Å and to grow along the [010] direction (Fig. 2b). XRD analysis (Fig. 1d) confirmed the Pd_2Sn NRs and spherical NPs to have the orthorhombic crystal structure (JCPDS 00-026-1297) and showed Pd NPs to have the cubic phase (JCPDS 01-088-2335). Within its experimental error, EDS analysis revealed metal ratios of Pd and Sn to be $[Pd]/[Sn] = 2.0 \pm 0.1$. In contrast, XPS analysis systematically provided significantly higher Sn contents, $[Pd]/[Sn] = 1.25 \pm 0.05$, which pointed toward a partial surface segregation of Sn.

Fig. 3 shows the Pd 3d and Sn 3d regions of the XPS spectrum of Pd_2Sn NRs. Pd 3d peaks could be deconvoluted into a pair of

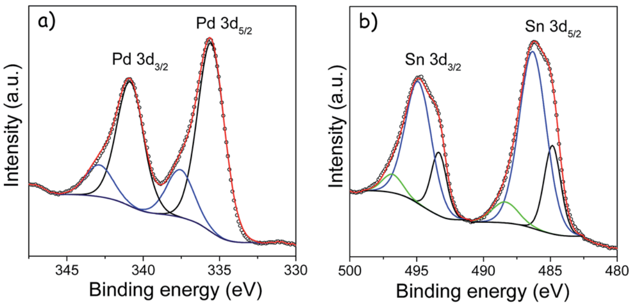

Fig. 3 Pd 3d and Sn 3d regions of the XPS spectrum of Pd_2Sn NRs.

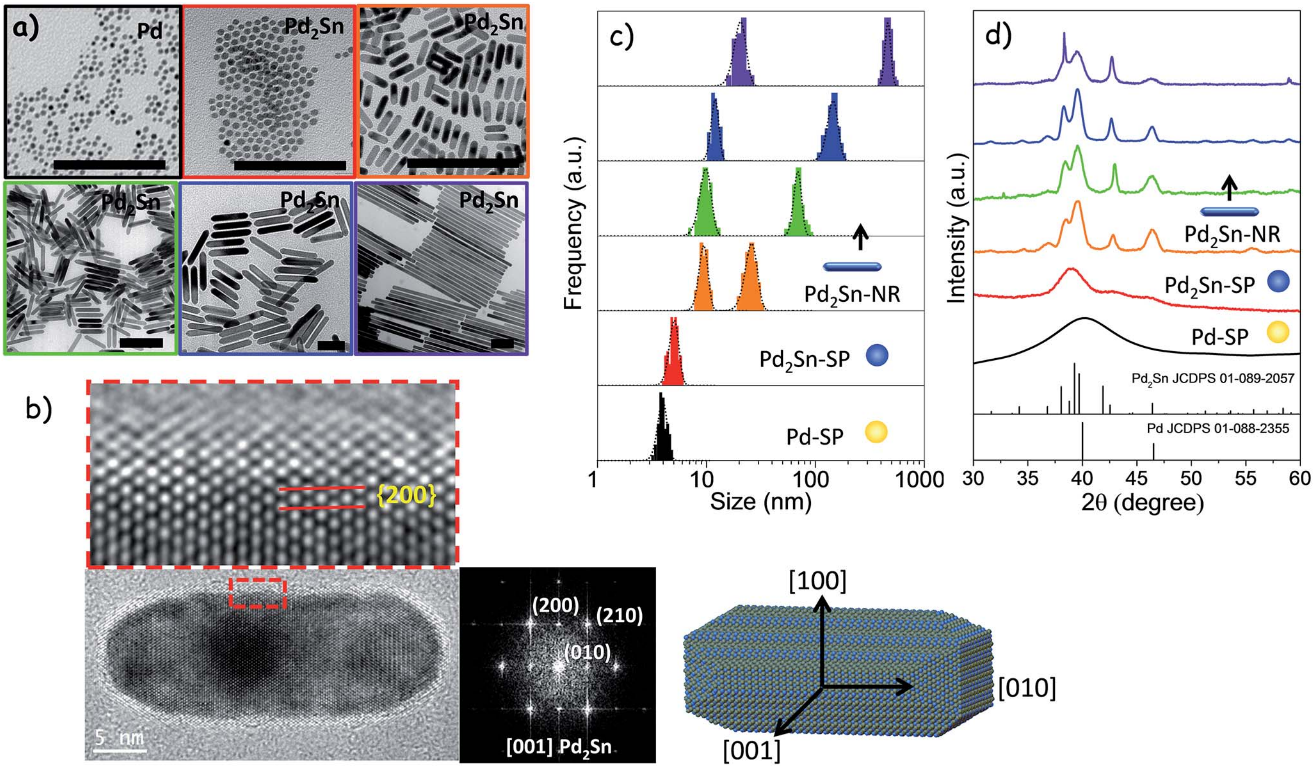

Fig. 2 (a) Representative TEM micrographs of spherical Pd NPs (4 nm), spherical Pd_2Sn NPs (5 nm) and Pd_2Sn NRs with different sizes: 9 nm × 26 nm; 10 nm × 70 nm; 12 nm × 150 nm; 20 nm × 460 nm. (b) HRTEM micrograph of a Pd_2Sn NR visualized along the [001] axis and its corresponding power spectrum, which shows that it has the orthorhombic Pd_2Sn phase. An atomic model of a Pd_2Sn NR is also displayed. (c) Size distribution histograms of the same samples; (d) XRD patterns including reference patterns of Pd (JCDPS 01-088-2355) and Pd_2Sn (JCDPS 01-089-2057).

doublets, pointing to the presence of two Pd chemical states. The main component, Pd^0, appeared at binding energies of 335.6 eV ($3d_{5/2}$) and 340.9 eV ($3d_{3/2}$), which represents a positive shift of ~0.5 eV compared with Pd metal, at 335.1 eV ($3d_{5/2}$) and 340.4 eV ($3d_{3/2}$). This result revealed that the electronic structure of Pd changed with the incorporation of Sn, which is a common observation considered to have a positive effect on catalytic activity by reducing the adsorption strength of poisonous intermediates.[48] On the other hand, the minority Pd^{2+} state provided peaks located at 337.6 eV ($3d_{5/2}$) and 342.9 eV ($3d_{3/2}$). In addition, three pairs of doublets were fitted to the Sn 3d binding energy region. The peaks at 488.4 eV ($3d_{5/2}$) and 496.8 eV ($3d_{3/2}$) were associated with Sn^{4+}, the stronger peaks at 486.3 eV ($3d_{5/2}$) and 494.9 eV ($3d_{3/2}$) could be associated with Sn^{2+}, and the minority component at 484.8 eV ($3d_{5/2}$) and 493.3 eV ($3d_{3/2}$) corresponded to metallic Sn. Thus Sn atoms on the Pd_2Sn NR surface appeared to be significantly oxidized as commonly observed in previous studies on Sn-based alloys.[21,49]

Control over the NP size and shape relies on the use of organic ligands adjusting surface energy and providing stability in solution. Such ligands may block catalytically active sites and hinder charge transfer, and thus they must be removed before testing the material electrocatalytic performance.[50,51] Several strategies have been proposed to clean colloidal NP surfaces, including the ligand decomposition by means of thermal annealing[52] or UV-ozone irradiation, surface etching and ligand exchange procedures.[53] In the present work, to remove the loosely bond OLA from the NP surface, NPs were suspended in a hydrazine hydrate aqueous/hexane two phase mixture. After shaking, the NPs moved into the polar phase leaving surfactants in the organic phase, as confirmed by the FTIR analysis (Fig. 4).

For electrocatalytic measurements, Pd and Pd_2Sn NPs were supported on GC. CV of the electrocatalysts prepared from Pd and Pd_2Sn spheres (Pd-SP/C and Pd_2Sn-SP/C) and from Pd_2Sn NRs (Pd_2Sn-NRs/C) was first investigated in 0.5 M KOH without ethanol (Fig. 5a and b). All NPs showed similar voltammetric profiles, although small differences in relevant regions of the voltammograms were observed. The peaks in the region between −0.6 V and −0.8 V *vs.* Hg/HgO are attributed to the absorption/adsorption and desorption of hydrogen. In the anodic sweep, the cyclic voltammetry of Pd_2Sn-NRs/C shows two peaks centered at −0.65 V and −0.41 V *vs.* Hg/HgO, attributed to the desorption of weakly and strongly bound hydrogen, respectively.

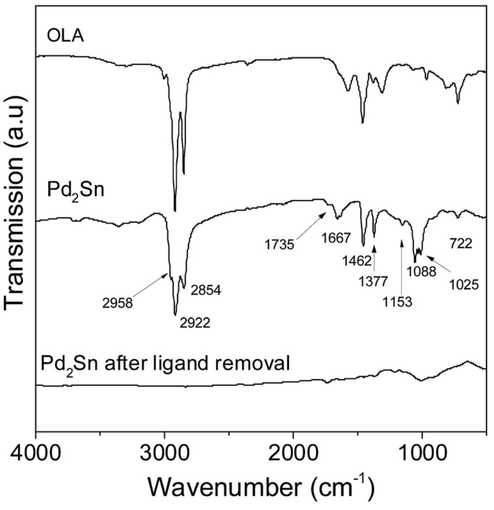

Fig. 4 FTIR spectra of OLA and Pd_2Sn NRs before and after ligand removal.

Moving to higher potentials, oxidation peaks associated with the formation of surface oxides appeared (from −0.4 to 0.1 V *vs.* Hg/HgO). Subsequently, oxide reduction peaks showed up during the negative scans (from 0 to −0.4 V *vs.* Hg/HgO). Comparing the cathodic peak potentials of Pd_2Sn- and Pd-based electrocatalysts, Pd_2Sn-NR/C samples showed positive shifts, indicating that the electronic structure of Pd atoms on the Pd_2Sn surface had changed, as observed from the XPS analysis. The electrochemically active surface area (ECSA) was estimated for all catalysts using the area over the voltammetry curve in the PdO_x reduction peak region (Table 2). The ECSA values increased when decreasing the NR length in Pd_2Sn-NRs/C catalysts, consistently with the increase of the surface area. Moreover, higher ECSA values were obtained for Pd-SP/C compared with most Pd_2Sn-based catalysts.

The EOR electrocatalytic activities were characterized by the CV technique in a mixture of 0.5 M KOH and 0.5 M ethanol aqueous solution (Fig. 5c and d). The hydrogen absorption–desorption peaks disappeared in the presence of the ethanol due to the dominant adsorption of the ethanol in the low-potential region. All CVs yielded a pair of well-defined peaks characteristic of the ethanol electro-oxidation. In the anodic scan, the forward oxidation peak at around 0.0 V *vs.* Hg/HgO is assigned to the oxidation of freshly chemisorbed species derived from ethanol adsorption. The current density decrease at high potentials is associated with the oxidation of the Pd surface blocking the EOR electrocatalytic activity. During the reverse scan, the catalyst reactivates when reaching the Pd reduction potentials (around −0.2 V *vs.* Hg/HgO). While the forward peak is associated with the dehydrogenation and dissociative adsorption of ethanol, the oxidation peak in the reverse scan has an additional strong contribution from the oxidation of carbonaceous species.[46]

To quantify the electrocatalytic performance, the redox onset potential (E_o), the forward oxidation current density peak (j_f), the potential at j_f (E_f), the backward anodic peak current (j_b) and the j_f/j_b ratio were determined (Table 2). Lower overpotentials and much higher current densities were generally obtained for the EOR in Pd_2Sn-based catalysts compared with Pd-SP/C. The overall EOR mechanism in alkaline media involves the reaction of ethanol with 4 OH^- groups to produce acetic acid and water. In Pd-based alloys, ethanol is generally accepted to adsorb at Pd sites. In Sn-based alloys, the formation of $Sn(OH)_x$ increases the surface density of OH^- groups available for ethanol oxidation, enhancing in this way the electrocatalytic activity.[21] On top of the alloying benefits, the rod geometry further reduced the overpotentials required, down to −0.47 V *vs.* Hg/HgO for Pd_2Sn-SP/C (9 × 26 nm) as compared with −0.39 for Pd-SP/C, and increased the peak current densities, up to 45.6 mA cm^{-2} (9 ×

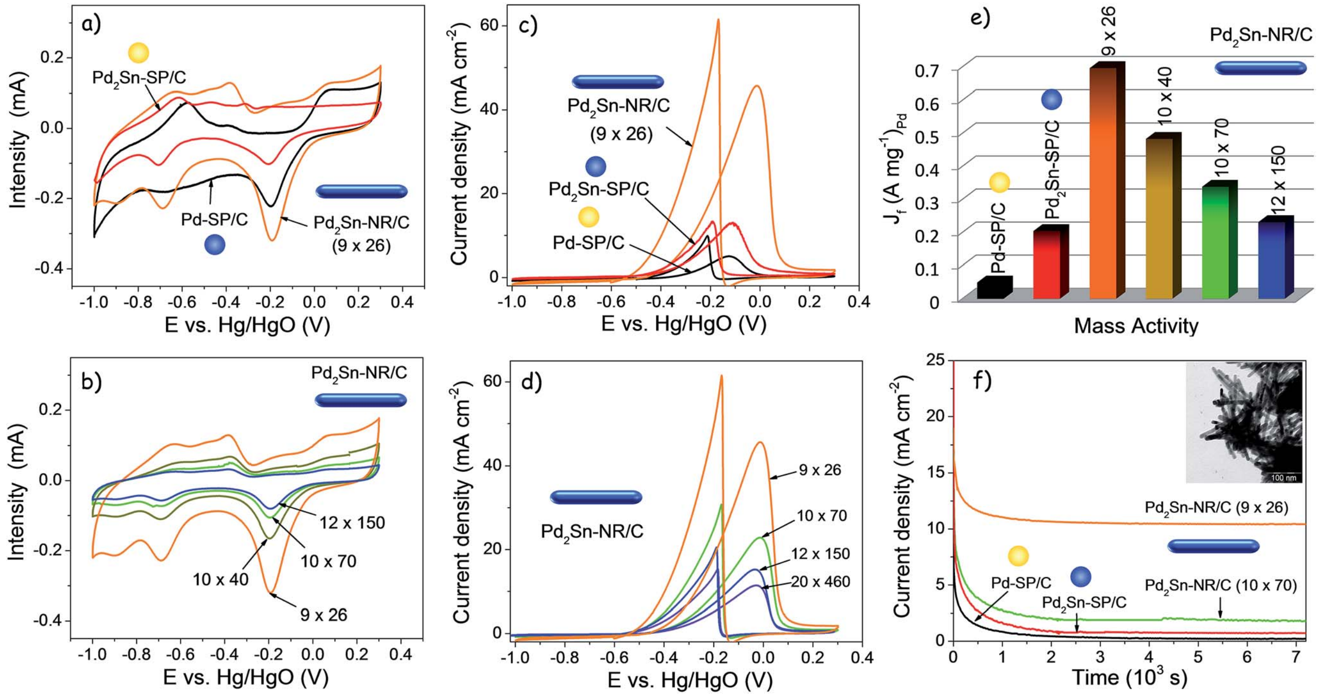

Fig. 5 (a–d) Cyclic voltammetric measurements of Pd and Pd_2Sn spheres and Pd_2Sn NRs with different sizes supported on GC in a 0.5 M KOH solution (a, b) and in a 0.5 M KOH + 0.5 M ethanol solution (c, d). (e) Mass activity at the ethanol oxidation peak calculated per mass of palladium. (f) Chronoamperometric measurements of the different samples in a 0.5 M KOH + 0.5 M ethanol solution at −0.1 V *vs.* Hg/HgO. The inset shows a TEM image of the 10 × 70 nm Pd_2Sn NRs after the stability test.

26 nm) as compared with 5.0 mA cm^{-2} and 13.1 mA cm^{-2} of Pd-SP/C and Pd_2Sn-SP/C, respectively. The lower onset potential measured from Pd_2Sn NRs compared with spherical Pd_2Sn NPs suggests lower activation energy for ethanol oxidation at the facets of Pd_2Sn NRs. Nevertheless, as the NR size increased, the current density decreased due to a reduction of the surface-to-bulk ratio as the thickness of the NRs also increased with the length. A decrease of the overall concentration of NR tips, potentially providing high activity sites, with the NR size increase may also contribute to the observed activity reduction. Overall the highest mass activity was obtained for the smallest Pd_2Sn NRs (9 × 26 nm Pd_2Sn-NRs/C), being 3 times higher than that of Pd_2Sn-SP/C and close to 10 times higher than that of Pd-SP/C (Table 2 and Fig. 5e).

Higher j_f/j_b ratios were obtained for all the Pd_2Sn-based catalysts when compared with Pd-SP/C, which is indicative of a more efficient oxidation of ethanol and less accumulation of carbonaceous species on the catalyst. The long-term stability of the electrocatalyst was determined by chronoamperometric techniques (Fig. 5f) at −0.1 V *vs.* Hg/HgO for 2 h. The current density of ethanol oxidation dropped quickly within the first seconds presumably due to the formation of strongly adsorbed intermediates on the surface of reactive sites. After that, the current decreased slowly and reached a pseudo-steady state. Current densities decayed faster on Pd NP-based electrodes than on Pd_2Sn NRs. After 2 h of reaction, the current obtained for Pd_2Sn-NR/C (10.4 mA cm^{-2}) was up to an order of magnitude higher than that of Pd_2Sn-SP/C (0.8 mA cm^{-2}) and Pd-SP/C (0.35

Table 2 Summary of the electrochemical parameters measured for Pd_2Sn-NR/C, Pd_2Sn-SP/C and Pd-SP/C electrocatalysts

Catalyst	ECSA (m^2 g^{-1})	E_o (V *vs.* Hg/HgO)	E_f (V *vs.* Hg/HgO)	j_f (mA cm^{-2})	j_f mass activity (A g^{-1})	$j_{-0.1\ V}$ (mA cm^{-2})	j_f/j_b	$j_{-0.1\ V}$ at 2 h (mA cm^{-2})	Tafel slope (mV dec^{-1})
Pd-SP/C	52.0	−0.39	−0.12	5.0	49	4.7	0.54	0.3	167
PdSn-SP/C	27.1	−0.51	0.11	13.1	131	12.8	0.98	0.8	128
Pd_2Sn-NR/C (9 × 26)	99.4	−0.47	−0.01	45.6	447	33.1	0.75	10.4	131
Pd_2Sn-NR/C (10 × 40)	54.3	−0.48	0.04	31.6	310	19.3	0.77	—	—
Pd_2Sn-NR/C (10 × 70)	33.9	−0.49	0.03	22.1	217	18.4	0.73	1.9	—
Pd_2Sn-NR/C (12 × 150)	22.6	−0.54	−0.04	15.1	148	17.1	0.75	—	—

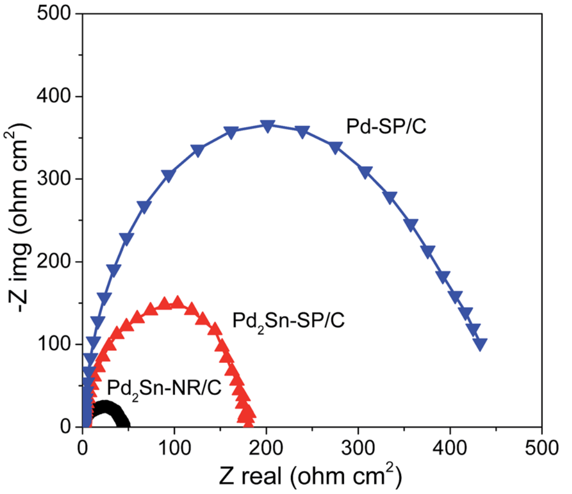

Fig. 6 Nyquist plot of the ethanol oxidation on Pd-SP/C, Pd_2Sn-SP/C and Pd_2Sn-NRs/C electrodes in a 0.5 M KOH + 0.5 M ethanol solution at −0.1 V *vs.* Hg/HgO.

mA cm^{-2}), proving the potential of Pd_2Sn NRs to enhance both performance and stability. TEM analysis of the NRs after the stability test showed no change in their size and geometry (Fig. 5f inset). Additional SEM-EDX analysis showed no change of their composition.

The linear region of the Tafel plots stretched from −0.4 to −0.1 V. As the potential is further increased above −0.2 V, the Tafel plot becomes curved, indicating that the EORs are no longer charge transfer controlled reactions. Similar Tafel slopes were obtained for the different Pd_2Sn-based catalysts, around 130 mV dec^{-1}, denoting a similar ethanol oxidation mechanism. These values significantly differed from that of Pd-SP/C (167 mV dec^{-1}) which also showed a clear change of the slope denoting a variation of the EOR mechanism. The lowest Tafel slopes obtained for the Pd_2Sn-based catalysts compared with Pd-SP/C can be explained by the contribution of Sn to form oxygenated species (*e.g.*, OH_{ads}) that participate in the EOR accelerating the oxidation of the reaction intermediates adsorbed on the Pd sites.

Fig. 6 displays the Nyquist impedance spectra of ethanol oxidation on Pd-SP/C, Pd_2Sn-SP/C and Pd_2Sn-NR/C electrodes. The measurements were made in a 0.5 M KOH + 0.5 M ethanol solution at −0.1 V *vs.* Hg/HgO. We observed the electron-transfer resistance of ethanol electrochemical oxidation to decrease in the following order: Pd-SP/C $\gg$ Pd_2Sn-SP/C $\gg$ Pd_2Sn-NR/C, demonstrating the enhanced electron-transfer kinetics of Pd_2Sn-NR/C catalysts, in good agreement with the voltammetric results presented above.

Conclusions

In summary, a series of Pd_2Sn NRs grown in the [010] direction were produced *via* colloidal synthesis routes. Their surface chemistry was characterized by XPS, which discerned a loosely bound organic shell that could be easily removed. Such NRs were employed as an electrocatalyst for the EOR in alkaline solution. Pd_2Sn NR-based electrocatalysts showed superior electrocatalytic activity and durability toward the EOR over Pd_2Sn and Pd nanospheres. The excellent electrocatalytic performance correlates with DFT calculations showing (001) and (100) facets to be more favorable than (010) facets for ethanol and OH adsorption, although further detailed surface analysis and much more meticulous DFT calculations taking into account all the reaction steps and the real Pd_2Sn NR surface, *i.e.* taking into account the higher amount of Sn observed and its possible surface ordering with Pd, are required to determine the exact EOR mechanism on this material.

Acknowledgements

This work was supported by the European Regional Development Funds and the Spanish MINECO project BOOSTER, TNT-FUELS, and PEC-CO_2. ZL thanks the China Scholarship Council for scholarship support. MI thanks AGAUR for Beatriu de Pinós postdoctoral grant (2013 BP-A00344). JL is a Serra Húnter Fellow and is grateful to the ICREA Academia program. The authors also acknowledge the funding from Generalitat de Catalunya 2014 SGR 1638.

Notes and references

1 Y.-J. Wang, J. Qiao, R. Baker and J. Zhang, *Chem. Soc. Rev.*, 2013, **42**, 5768–5787.

2 M. Akhairi and S. K. Kamarudin, *Int. J. Hydrogen Energy*, 2016, **41**, 4214–4228.

3 Y. Chen, M. Bellini, M. Bevilacqua, P. Fornasiero, A. Lavacchi, H. A. Miller, L. Wang and F. Vizza, *ChemSusChem*, 2015, **8**, 524–533.

4 M. Kamarudin, S. K. Kamarudin, M. Masdar and W. R. W. Daud, *Int. J. Hydrogen Energy*, 2013, **38**, 9438–9453.

5 L. An and T. Zhao, *Energy Environ. Sci.*, 2011, **4**, 2213–2217.

6 E. Antolini and E. R. Gonzalez, *J. Power Sources*, 2010, **195**, 3431–3450.

7 S. Badwal, S. Giddey, A. Kulkarni, J. Goel and S. Basu, *Appl. Energy*, 2015, **145**, 80–103.

8 J. R. Varcoe, R. C. Slade, E. L. H. Yee, S. D. Poynton and D. J. Driscoll, *J. Power Sources*, 2007, **173**, 194–199.

9 N. J. Robertson, H. A. Kostalik IV, T. J. Clark, P. F. Mutolo, H. D. Abruña and G. W. Coates, *J. Am. Chem. Soc.*, 2010, **132**, 3400–3404.

10 R. B. Kutz, B. r. Braunschweig, P. Mukherjee, D. D. Dlott and A. Wieckowski, *J. Phys. Chem. Lett.*, 2011, **2**, 2236–2240.

11 V. Rao, C. Cremers and U. Stimming, *Fuel Cells*, 2007, **7**, 417–423.

12 C. Busó-Rogero, S. Brimaud, J. Solla-Gullon, F. J. Vidal-Iglesias, E. Herrero, R. J. Behm and J. M. Feliu, *J. Electroanal. Chem.*, 2016, **763**, 116–124.

13 A. Bach Delpeuch, F. Maillard, M. Chatenet, P. Soudant and C. Cremers, *Appl. Catal., B*, 2016, **181**, 672–680.

14 Y. Wang, S. Zou and W.-B. Cai, *Catalysts*, 2015, **5**, 1507.

15 D. A. Cantane, W. F. Ambrosio, M. Chatenet and F. H. B. Lima, *J. Electroanal. Chem.*, 2012, **681**, 56–65.

16 Y.-J. Wang, N. Zhao, B. Fang, H. Li, X. T. Bi and H. Wang, *Chem. Rev.*, 2015, **115**, 3433–3467.
17 W. J. Zhou, S. Q. Song, W. Z. Li, G. Q. Sun, Q. Xin, S. Kontou, K. Poulianitis and P. Tsiakaras, *Solid State Ionics*, 2004, **175**, 797–803.
18 S. Carrión-Satorre, M. Montiel, R. Escudero-Cid, J. L. G. Fierro, E. Fatás and P. Ocón, *Int. J. Hydrogen Energy*, 2016, **41**, 8954–8962.
19 C. Bianchini and P. K. Shen, *Chem. Rev.*, 2009, **109**, 4183–4206.
20 H. An, L. Pan, H. Cui, B. Li, D. Zhou, J. Zhai and Q. Li, *Electrochim. Acta*, 2013, **102**, 79–87.
21 W. Du, K. E. Mackenzie, D. F. Milano, N. A. Deskins, D. Su and X. Teng, *ACS Catal.*, 2012, **2**, 287–297.
22 L.-X. Ding, A.-L. Wang, Y.-N. Ou, Q. Li, R. Guo, W.-X. Zhao, Y.-X. Tong and G.-R. Li, *Sci. Rep.*, 2013, **3**, 1181.
23 A. N. Geraldes, D. Furtunato da Silva, J. C. Martins da Silva, O. Antonio de Sá, E. V. Spinacé, A. O. Neto and M. Coelho dos Santos, *J. Power Sources*, 2015, **275**, 189–199.
24 Z. Luo, M. Ibáñez, A. M. Antolín, A. Genç, A. Shavel, S. Contreras, F. Medina, J. Arbiol and A. Cabot, *Langmuir*, 2015, **31**, 3952–3957.
25 A.-L. Wang, X.-J. He, X.-F. Lu, H. Xu, Y.-X. Tong and G.-R. Li, *Angew. Chem., Int. Ed.*, 2015, **54**, 3669–3673.
26 H. Na, L. Zhang, H. Qiu, T. Wu, M. Chen, N. Yang, L. Li, F. Xing and J. Gao, *J. Power Sources*, 2015, **288**, 160–167.
27 J. Yin, S. Shan, M. S. Ng, L. Yang, D. Mott, W. Fang, N. Kang, J. Luo and C.-J. Zhong, *Langmuir*, 2013, **29**, 9249–9258.
28 J. Cai, Y. Huang and Y. Guo, *Electrochim. Acta*, 2013, **99**, 22–29.
29 A. Shavel, M. Ibáñez, Z. Luo, J. De Roo, A. Carrete, M. Dimitrievska, A. Genç, M. Meyns, A. Pérez-Rodríguez and M. V. Kovalenko, *Chem. Mater.*, 2016, **28**, 720–726.
30 W. Li, R. Zamani, P. Rivera Gil, B. Pelaz, M. Ibáñez, D. Cadavid, A. Shavel, R. A. Alvarez-Puebla, W. J. Parak and J. Arbiol, *J. Am. Chem. Soc.*, 2013, **135**, 7098–7101.
31 M. Ibáñez and A. Cabot, *Science*, 2013, **340**, 935–936.
32 M. Ibáñez, R. Zamani, S. Gorsse, J. Fan, S. Ortega, D. Cadavid, J. R. Morante, J. Arbiol and A. Cabot, *ACS Nano*, 2013, **7**, 2573–2586.
33 R. Nafria, A. Genç, M. Ibáñez, J. Arbiol, P. Ramírez de la Piscina, N. Homs and A. Cabot, *Langmuir*, 2016, **32**, 2267–2276.
34 X. Yu, J. Liu, A. Genç, M. Ibáñez, Z. Luo, A. Shavel, J. Arbiol, G. Zhang, Y. Zhang and A. Cabot, *Langmuir*, 2015, **31**, 10555–10561.
35 X. Yu, A. Shavel, X. An, Z. Luo, M. Ibáñez and A. Cabot, *J. Am. Chem. Soc.*, 2014, **136**, 9236–9239.
36 Z. Luo, E. Irtem, M. Ibáñez, R. Nafria, S. Martí-Sánchez, A. Genç, M. de la Mata, Y. Liu, D. Cadavid, J. Llorca, J. Arbiol, T. Andreu, J. R. Morante and A. Cabot, *ACS Appl. Mater. Interfaces*, 2016, **8**, 17435–17444.
37 R. R. Zamani, M. Ibáñez, M. Luysberg, N. García-Castelló, L. Houben, J. D. Prades, V. Grillo, R. E. Dunin-Borkowski, J. R. Morante, A. Cabot and J. Arbiol, *ACS Nano*, 2014, **8**, 2290–2301.
38 G. Kresse and J. Hafner, *Phys. Rev. B: Condens. Matter Mater. Phys.*, 1993, **47**, 558–561.
39 G. Kresse and J. Furthmuller, *Comput. Mater. Sci.*, 1996, **6**, 15–50.
40 G. Kresse and D. Joubert, *Phys. Rev. B: Condens. Matter Mater. Phys.*, 1999, **59**, 1758–1775.
41 J. P. Perdew and Y. Wang, *Phys. Rev. B: Condens. Matter Mater. Phys.*, 1986, **33**, 8800–8802.
42 J. P. Perdew and Y. Wang, *Phys. Rev. B: Condens. Matter Mater. Phys.*, 1992, **45**, 13244–13249.
43 S. Grimme, J. Antony, S. Ehrlich and H. Krieg, *J. Chem. Phys.*, 2010, **132**, 154104.
44 S. A. Kirillov, P. E. Tsiakaras and I. V. Romanova, *J. Mol. Struct.*, 2003, **651–653**, 365–370.
45 E. D. Wang, J. B. Xu and T. S. Zhao, *J. Phys. Chem. C*, 2010, **114**, 10489–10497.
46 Z. Liang, T. Zhao, J. Xu and L. Zhu, *Electrochim. Acta*, 2009, **54**, 2203–2208.
47 A. Kowal, M. Li, M. Shao, K. Sasaki, M. Vukmirovic, J. h. Zhang, N. Marinkovic, P. Liu, A. Frenkel and R. Adzic, *Nat. Mater.*, 2009, **8**, 325–330.
48 Z. Zhang, J. Ge, L. Ma, J. Liao, T. Lu and W. Xing, *Fuel Cells*, 2009, **9**, 114–120.
49 Y. Feng, D. Bin, K. Zhang, F. Ren, J. Wang and Y. Du, *RSC Adv.*, 2016, **6**, 19314–19321.
50 D. V. Talapin, J.-S. Lee, M. V. Kovalenko and E. V. Shevchenko, *Chem. Rev.*, 2010, **110**, 389–458.
51 T. Chen and V. O. Rodionov, *ACS Catal.*, 2016, **6**, 4025–4033.
52 M. Ibáñez, Z. Luo, A. Genç, L. Piveteau, S. Ortega, D. Cadavid, O. Dobrozhan, Y. Liu, M. Nachtegaal and M. Zebarjadi, *Nat. Commun.*, 2016, **7**, 10766.
53 Z. Niu and Y. Li, *Chem. Mater.*, 2014, **26**, 72–83.